CHIN. PHYS. LETT. Vol. 38, No. 8 (2021) 087702

Ferroelectric Controlled Spin Texture in Two-Dimensional $NbOI_2$ Monolayer

Qian Ye(叶倩)[1†], Yu-Hao Shen(沈宇皓)[1†], and Chun-Gang Duan(段纯刚)[1,2*]

[1]*State Key Laboratory of Precision Spectroscopy and Key Laboratory of Polar Materials and Devices (Ministry of Education), Department of Electronics, East China Normal University, Shanghai 200241, China*
[2]*Collaborative Innovation Center of Extreme Optics, Shanxi University, Taiyuan 030006, China*

(Received 23 April 2021; accepted 14 July 2021; published online 2 August 2021)

The persistent spin helix (PSH) system is considered to have promising applications in energy-conservation spintronics because it supports an extraordinarily long spin lifetime of carriers. Here, we predict that the existence of PSH state in two-dimensional (2D) ferroelectric $NbOI_2$ monolayers. Our first-principles calculation results show that there exists Dresselhaus-type spin-orbit coupling (SOC) band splitting near the conduction-band minimum (CBM) of the $NbOI_2$ monolayer. It is revealed that the spin splitting near CBM merely refers to out-of-plane spin configuration in the wave vector space, which gives rise to a long-lived PSH state that can be controlled by reversible ferroelectric polarization. We believe that the coupling characteristics of ferroelectric polarization and spin texture in $NbOI_2$ provide a platform for the realization of fully electric controlled spintronic devices.

DOI: 10.1088/0256-307X/38/8/087702

In recent years, a series of peculiar physical achievement related to relativistic spintronics have been discovered. Such as spin-orbit torques,[1] spin Hall effect,[2−4] and spin-valley physics,[5−8] making the development of condensed matter physics vigorous. Spin-orbit coupling (SOC) plays a vital role in the generation of these special phenomena and properties.[9,10] Such research goal of spintronics is to make use of these special and interesting effects and phenomena to achieve the control of the spin degree of freedom extensively. As we know, when electrons move in a system with broken spatial inversion symmetry, there will perceive an effective momentum $\boldsymbol{k}$ dependent magnetic field as a matter of relativistic effect, so that the spin of the electron spin will not be conserved.[11] This phenomenon is the result of the coupling between the electron's momentum and its spin. The corresponding Hamiltonian can be expressed as[12]

$$H_{\rm so} = \boldsymbol{\Omega}(\boldsymbol{k}) \cdot \boldsymbol{\sigma}, \tag{1}$$

where $\boldsymbol{\Omega}(\boldsymbol{k}) = \alpha(|\boldsymbol{E}|)(\hat{E} \times \boldsymbol{k})$ is defined as the spin-orbit field (SOF), α is the strength of the SOC which depends on the magnitude of the local electric field $\boldsymbol{E}$ induced by the spatial inversion symmetry breaking, and $\boldsymbol{\sigma} = (\sigma_x \sigma_y \sigma_z)$ is the Pauli matrices vector. The $\boldsymbol{\Omega}(\boldsymbol{k})$ possesses odd parity,[13] therefore the SOC lifts Kramer's spin degeneracy and leads to a complex $\boldsymbol{k}-$dependent pseudospin texture in the $\boldsymbol{k}$ space, which is usually hidden in solid system.[14]

It is more noteworthy that under an external electric field, the direction of the ferroelectric polarization can be reversed. Significantly, the control of ferroelectric field achieves non-volatile regulation of the charge polarization state, spin splitting and even the spin texture in the momentum space.[15] Based on this spirit, with the development of two-dimensional ferroelectric materials,[16,17] a new ferroelectric Rashba semiconductor was proposed.[18] The interplay of spin texture and ferroelectric polarization, allows a non-volatile way of electric manipulation towards the spin degree of freedom. It realizes many spintronic device applications such as spin field effect transistors.[19]

Sante *et al.* firstly established the relationship between the Rashba effect and the ferroelectric field in single-phase materials. Based on first principles calculations the giant Rashba effect in the narrow bandgap ferroelectric semiconductor GeTe is theoretically predicted.[20] Experimentally the significant Rashba effect due to the ferroelectric polarization in α-GeTe(111) is observed.[21,22] Similarly, a series of studies on ferroelectric Rashba semiconductors have been developed: bulk ferroelectric materials $BiAlO_3$,[23] HfO_2,[24] $PbTiO_3$[25] and two-dimensional bilayer or multilayer elemental Te,[26] $AgBiP_2X_6$ (X = S, Se, Te) monolayer.[27]

However, in a system with SOC effect, spin rotation symmetry is usually broken. Electron spin rotates or even flips as a result of electron scattering and the corresponding phenomenon belongs to the

Supported by the National Key Research and Development Program of China (Grant No. 2017YFA0303403), the Shanghai Science and Technology Innovation Action Plan (Grant No. 19JC1416700), the National Natural Science Foundation of China (Grant No. 11774092), and the ECNU Multifunctional Platform for Innovation.
†They contributed equally to this work.
*Corresponding author. Email: cgduan@clpm.ecnu.edu.cn
© 2021 Chinese Physical Society and IOP Publishing Ltd

D'yakonov-perel'-Kachorovskii (DPK) spin relaxation mechanism.[28,29] Undoubtedly, DPK spin relaxation interferes with the spin precession of electrons, weakens the electron spin polarization, shortens the spin lifetime, and will has a negative influence on the potential performance of spintronic devices. In order to effectively solve the problem of DPK spin relaxation, there proposes two corresponding theoretical methods to configuration a unidirectional spin: to make the coupling strength coefficient α_{R} of Rashba effect equal to that α_{D} of Dresselhaus effect, or to make use of pure Dresselhaus SOC described by the [110] quantum-well Dresselhaus model.[30]

In this Letter, based on first-principles calculations, combined with an effective $\boldsymbol{k}\cdot\boldsymbol{p}$ model analysis, we find that there is a significant Dresselhaus-type band splitting near the conduction band minimum (CBM) of the 2D in-plane ferroelectric material XOI_2 monolayer. A typical monolayer system VOI_2 has been reported to possess such ferroelectricity[31–33] and we then replace V to Nb to reveal that the spin configuration near CBM of the $NbOI_2$ monolayer merely possesses out-of-plane components, generating a long-lived PSH state for the electron spin under an effective magnetic field.[34–36] More interestingly, the coupling between the spin and the ferroelectric polarization achieves reversible spin texture in such a system. Our results indicate the possibility of realizing non-volatile electrically controlled spin texture in a 2D ferroelectric material $NbOI_2$ monolayer, providing a platform for designing high-performance ferroelectric and spintronic devices.

Method. We perform our first-principles calculation based on the Vienna *ab initio* simulation package (VASP).[37] The electron-ion interactions were handled by the projector augmented wave (PAW) method.[38] The exchange correlation potential is treated in Perdew–Burke–Ernzerhof (PBE) form of the generalized gradient approximation (GGA). A vacuum layer with a thickness of 20 Å was used to avoid artificial interactions between neighboring layers, and an energy cutoff of 520 eV was set for the plane-wave basis. Meanwhile, the Brillouin zone (BZ) integration was sampled with a k-grid density of $11\times7\times1$ using the Monkhorst–Pack scheme.[39] The structures were fully optimized until the maximal forces were less than 0.005 eV/Å and the convergence criteria for energy was set to be 10^{-6} eV. The spontaneous ferroelectric polarization was calculated by the Berry phase approach, in which both electronic and ionic contributions were taken into account.[40,41] The calculation of the phonon spectrum was performed using the finite displacement method which was implemented in Phonopy.[42] We expanded the 8-atom unit cell to a 128-atom supercell, while k-grid density is used with $2\times2\times1$ and the convergence criterion of energy is set to 10^{-8} eV. The minimum energy pathways of ferroelectric transitions were determined through the climbing image nudged elastic band (CINEB) method[43] based on the interatomic forces and total energies acquired from the DFT calculations.

Results and Discussion. The ferroelectric phase of the $NbOI_2$ monolayer has space group of $Pmm2$.[44] In Figs. 1(a) and 1(b) we define a and b as lattice parameters along x and y axes, respectively. Our optimized lattice constants are $a = 3944$ Å and $b = 7583$ Å for ferroelectric $NbOI_2$ monolayer. The top and side views of $NbOI_2$ monolayer are shown in Figs. 1(a) and 1(b). The blue dotted frame is the unit cell structure of $NbOI_2$. It is clear that $Nb_2O_2I_4$ octahedron builds a 2D grid structure through the sharing of edges and corners. Each Nb atom is connected to two O atoms and four I atoms, trapped in an octahedron. Note that for the ferroelectric phase, the structural asymmetry lies on the fact that the Nb atom is not located at the center of the octahedron, but in the plane along the x axis, which is close to the O atom at one side and away from the other side, i.e., an off-center displacement. Here, the distance from the center of $NbOI_2$ along the x-axis is about 0.14 Å, which is in good agreement with the reported results.[44] The first Brillouin zone is shown in Fig. 1(c), in which we have marked the main high symmetry points (Γ, X, S, Y). As shown in Fig. 1(d), we calculated the phonon spectrum of ferroelectric phase $NbOI_2$ monolayer and found that there is no false frequency, indicating a dynamically stable structure of the ferroelectric $NbOI_2$.

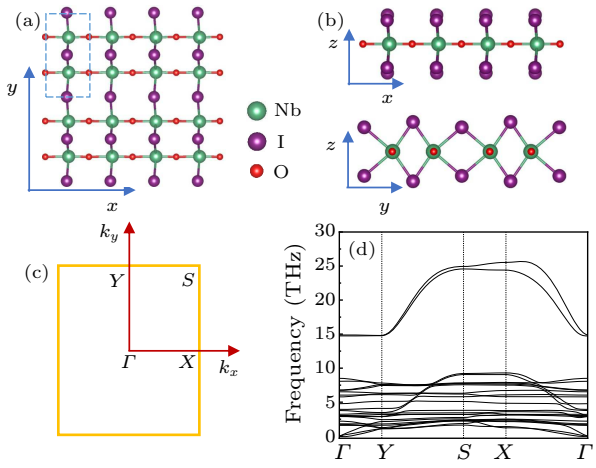

Fig. 1. The top view (a) and side view (b) of the $NbOI_2$ monolayer, respectively. The blue rectangle indicates the unit cell. Green, red and purple balls represent the Nb, O and I, respectively. (c) First Brillouin zone of the $NbOI_2$ monolayer characterized by high symmetry $\boldsymbol{k}$ points (Γ, X, S, Y) are shown. (d) The phonon spectra of the ferroelectric $NbOI_2$ monolayer.

Next, we calculated the ferroelectric polarization

of $NbOI_2$ monolayer using the Berry phase method. Figure 2(a) shows the variation of the total energy of the system with the normalized ferroelectric displacement λ. This is a typical ferroelectric double potential well energy diagram. The lowest points of energy correspond to the ferroelectric phase of the P_+ and P_- states, respectively. In Fig. 2(b) we show the switch of the ferroelectric polarization with the normalized ferroelectric displacement λ. It can be seen that the ferroelectric polarization is 142.5 pC/m. Considerably, this value is comparable with that of other 2D in-plane ferroelectric system such as the fourth main group monochalcogenide MX(M = Ge, Sn; X = S, Se) monolayer[45–48] (151–506 pC/m) and the WO_2Cl_2 monolayer[49] (189.8 pC/m).

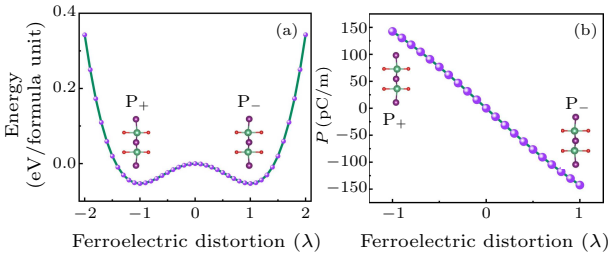

Fig. 2. (a) Total energy of the system and (b) polarization of $NbOI_2$ as a function of ferroelectric displacement λ, where $\lambda = +1$ and -1 correspond to the equivalent ferroelectric states P_+ and P_-.

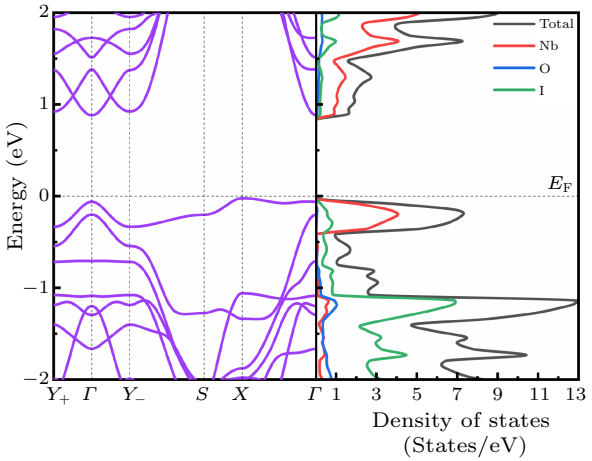

Fig. 3. Band structure diagram of $NbOI_2$ monolayer without considering the spin-orbit coupling effect and density of states diagram.

The calculated band structures of $NbOI_2$ monolayer without SOC effect is shown in the left side of Fig. 3. Significantly, it can be seen that when the SOC effect is not included, the bands of the $NbOI_2$ monolayer are spin-degenerate and the ferroelectric $NbOI_2$ monolayer is an indirect band gap (about 0.904 eV) semiconductor. In Ref. [44] the HSE functional method is used to obtain the value of band gap of 1.77 eV. This difference is just because the PBE method we use usually underestimates the value of the system, which is manifested to lift valence-band maximum (VBM) upwards and shift conduction-band maximum (CBM) downwards. And our results are that CBM and (VBM) are respectively located at the $\Gamma(0,0,0)$ and $X(0.5,0,0)$. It can be seen from the density of states diagram in the right side of Fig. 3 that the orbital components near CBM and VBM are mainly contributed by Nb atoms, while the contribution of O atoms and I atoms is relatively small.

Figures 4(a) and 4(b) show the band structures of the $NbOI_2$ monolayer with SOC effect considered. Compared with that in Fig. 3, VBM changes from $X(0.5,0,0)$ to $\Gamma(0,0,0)$, and correspondingly, the $NbOI_2$ monolayer becomes a direct bandgap semiconductor with a band gap value of 0.876 eV. In addition, with SOC effect taken into account, the bands near CBM split along k_y direction, as clearly shown in the insets of Figs. 4(a) and 4(b). It can be demonstrated that the splitting can be opposite under the reversal of ferroelectric polarization, meaning the reversal of spin polarization.

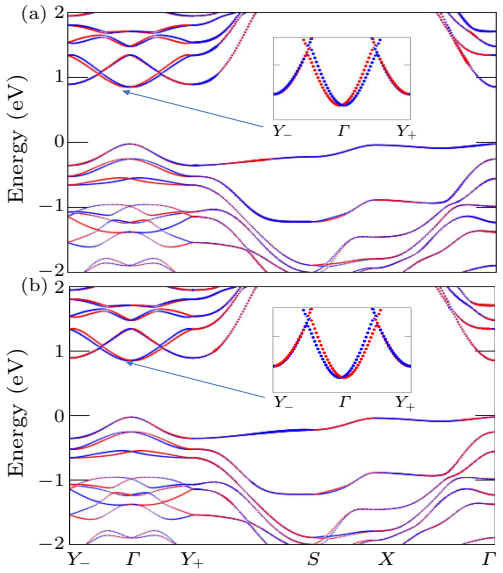

Fig. 4. Considering the SOC effect of the $NbOI_2$ monolayer (a) P_+ ferroelectric phase energy band diagram and (b) P_- ferroelectric phase energy band diagram. The small picture inserted in the energy band diagram is of the electron energy band structure near CBM on the Y_-–Γ–Y_+ path. The red and blue curves represent spin-up and spin-down, respectively.

The above flipping of spin polarization can be explained with an effective $\boldsymbol{k}\cdot\boldsymbol{p}$ model. In fact, the $NbOI_2$ monolayer belongs to the $Pmm2$ space group and has C_{2v} point group symmetry at point Γ, which contains four symmetry operations: identity element E and reflection M_y, M_z and a twofold rotation C_2, as shown in Fig. 5(a). The transformations that the wave vector $\boldsymbol{k}$ and Pauli matrix $\boldsymbol{\sigma}$ should satisfy under time reversal operator T and symmetric operation are shown in Table 1. We can see that under the time re-

versal and C_{2v} point group symmetry operation, only the $ky\sigma_z$ term remains invariant.

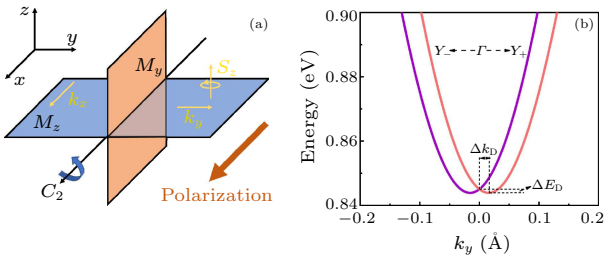

Fig. 5. (a) Schematic diagram of C_{2v} point group symmetry operation elements. (b) Schematic diagram of CBM band splitting of $NbOI_2$.

Table 1. The transformation form under the performance operation.[24]

Symmetry operation	k_x,k_y	$\sigma_x, \sigma_y, \sigma_z$
T	$(-k_x,-k_y)$	$(-\sigma_x,-\sigma_y,-\sigma_z)$
$C_2 = i\sigma_x$	$(k_x,-k_y)$	$(\sigma_x,-\sigma_y,-\sigma_z)$
$M_y = i\sigma_y$	$(k_x,-k_y)$	$(-\sigma_x,\sigma_y,-\sigma_z)$
$M_z = i\sigma_z$	(k_x,k_y)	$(-\sigma_x,-\sigma_y,\sigma_z)$

Consequently, the Hamiltonian of such a system can be written as[34,35]

$$H = E_0(k) + \alpha_{\mathrm{D}} k_y \sigma_z \tag{2}$$

where $E_0(k) = \hbar^2(k_x^2 + k_y^2)/2m^*$ is the kinetic energy and m^* is the effective mass; α_{D} is the Dresselhaus coupling coefficient. The z component of spin operator $\boldsymbol{S}$ is $S_z = \frac{\hbar}{2}\sigma_z$. The Hamiltonian H of the system is consistent with the Hamiltonian of the [110]-grown Ⅲ–V quantum wells.[35] The energy dispersions can be expressed as

$$E_{\pm} = E_0(k) \pm \alpha_{\mathrm{D}} k_y. \tag{3}$$

Because of $SU(2)$ symmetry, when S_z commutes with the Hamiltonian, $[S_z, H] = 0$, S_z is conserved. There almost exits one component S_z: $\langle S_{\pm}\rangle = (\langle S_x, S_y, S_z\rangle)_{\pm} = \frac{\hbar}{2}(0,0,1)$ in the entire 2D $\boldsymbol{k}$ space except for $k_y = 0$, which leads to a unidirectional spin configuration perpendicular to the plane in momentum space and then form the PSH state.

Next, we quantitatively analyze the spin splitting near the Γ point. The strength of the Dresselhaus effect α_{D} can be estimated using relations $\alpha_{\mathrm{D}} = \frac{2\Delta E_{\mathrm{D}}}{\Delta k_{\mathrm{D}}}$, where ΔE_{D} and Δk_{D} are the energy offset and wave vector offset, respectively [shown in Fig. 5(b)]. From the calculated band structures, we obtain $\Delta E_{\mathrm{D}} = 1.12\,\mathrm{meV}$, $\Delta k_{\mathrm{D}} = 0.017\,\mathrm{Å}^{-1}$, so $\alpha_{\mathrm{D}} = \frac{2\Delta E_{\mathrm{D}}}{\Delta k_{\mathrm{D}}} = 0.134\,\mathrm{eV{\cdot}Å}$, which is much smaller than that of a two-dimensional SnSe monolayer (0.76–1.15 eV·Å).[50]

In order to further verify the prediction of the above $\boldsymbol{k}\cdot\boldsymbol{p}$ model, we then calculated the spin polarization distribution as shown in Fig. 6(a) for the lowest conduction band.

What we can see is that the spin distribution merely contains out-of-plane components S_z. This result is in good agreement with Eq. (2). Therefore, the effective magnetic field $\boldsymbol{\Omega}(\boldsymbol{k})$ distribution near CBM is almost unidirectional, which indicates that it is very promising to realize PSH state and longer spin lifetime in such a monolayer system. Moreover, when the ferroelectric polarization is reversed, the direction of the spin polarization becomes opposite as shown in Fig. 6(a).

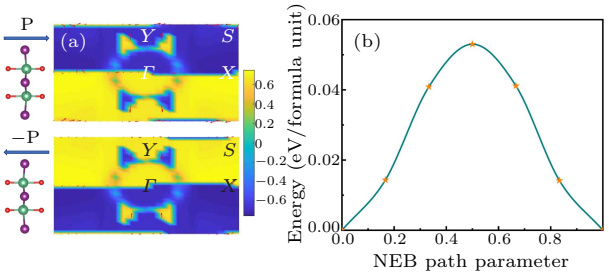

Fig. 6. (a) The spin polarization distribution of the first Brillouin zone in the opposite ferroelectric polarization state (red arrow represents the spin polarization distribution in the plane, yellow and blue blocks represent the out-of-plane spin polarization distribution, which are upward and downward, respectively). (b) Calculation of nudged elastic band in the process of polarization reversal of two ferroelectric phases with degenerate energy and equivalent structure through the paraelectric phase.

In fact, as ferroelectric polarization switched from $\boldsymbol{P}$ to $-\boldsymbol{P}$ the equivalently performs spatial inversion operation: $\boldsymbol{k}$ to $-\boldsymbol{k}$, but $\boldsymbol{\sigma}$ remains invariant.[51] However, under time reversal operation there appear reverses $-\boldsymbol{k}$ to $\boldsymbol{k}$, and $\boldsymbol{\sigma}$ to $-\boldsymbol{\sigma}$. Since the Bloch state $|+\boldsymbol{P},\boldsymbol{k}\rangle$ is reversed by the combined operation of the time inversion T and the space inversion I, i.e., $\boldsymbol{TI}|+\boldsymbol{P},\boldsymbol{k}\rangle = |-\boldsymbol{P},\boldsymbol{k}\rangle$, we have expectation values of spin operator $\langle S\rangle$:[51]

$$\begin{aligned}\langle S\rangle[-\boldsymbol{P},\boldsymbol{k}] &= \langle -\boldsymbol{P},\boldsymbol{k}\,|\,\boldsymbol{S}\,|\,-\boldsymbol{P},\boldsymbol{k}\rangle \\ &= \langle +\boldsymbol{P},\boldsymbol{k}\,|\,I^{-1}T^{-1}\boldsymbol{STI}\,|\,+\boldsymbol{P},\boldsymbol{k}\rangle \\ &= \langle +\boldsymbol{P},\boldsymbol{k}\,|\,-\boldsymbol{S}\,|\,+\boldsymbol{P},\boldsymbol{k}\rangle \\ &= \langle -S\rangle[+\boldsymbol{P},\boldsymbol{k}].\end{aligned} \tag{4}$$

This mainly explains why the spin polarization can be reversed with the reversal of the ferroelectric polarization. More importantly, we used the CINEB to calculate the minimum energy path of the ferroelectric polarization reversal. As shown in Fig. 6(b), we found that the path of the energy barrier to overcome for ferroelectric polarization reversal is 0.053 eV/formula unit, which seems to be larger than that in Ref. [44] (about 0.01 eV/formula unit). This is because in our case we fix the lattice constant that is equal to the value in ferroelectric phase. Anyway, according to the calculated results of CINEB and the reversible spin texture of the $NbOI_2$ system, it is demonstrated that

the PSH state controlled by the in-plane ferroelectric polarization can be realized in the $NbOI_2$ monolayer by an external electric field.

In summary, based on first-principles calculations, combined with symmetry and $\boldsymbol{k}\cdot\boldsymbol{p}$ model analysis, we have found that the $NbOI_2$ monolayer possesses both in-plane ferroelectricity and the Dresselhaus spin-orbit coupling effect, that is, the significant band splitting near CBM. Our calculation results reveal that the effective magnetic field is along z direction near the CBM, resulting in a unidirectional out-of-plane spin texture and forming a PSH state. It then inhibits the DPK spin relaxation mechanism. In addition, as the ferroelectric polarization is reversed, the spin texture is reversed correspondingly. Our findings show that the interplay between ferroelectric polarization and spin texture in $NbOI_2$ monolayer provides a platform for realization of fully electric control in spintronic devices design.

References

[1] Manchon A, Miron I, Jungwirth T, Sinova J, Zelezny J, Thiaville A, Garello K and Gambardella P 2019 *Rev. Mod. Phys.* **91** 035004
[2] Sinova J, Valenzuela S O, Wunderlich J, Back C H and Jungwirth T 2015 *Rev. Mod. Phys.* **87** 1213
[3] Kane C L and Mele E J 2005 *Phys. Rev. Lett.* **95** 226801
[4] Bernevig B A and Zhang S C 2006 *Phys. Rev. Lett.* **96** 106802
[5] Xu X, Yao W, Xiao D and Heinz T F 2014 *Nat. Phys.* **10** 343
[6] Schaibley J R, Yu H, Clark G, Rivera P, Ross J S, Seyler K L, Yao W and Xu X 2016 *Nat. Rev. Mater.* **1** 16055
[7] Tong W Y, Gong S J, Wan X and Duan C G 2016 *Nat. Commun.* **7** 13612
[8] Hu H, Tong W Y, Shen Y H and Duan C G 2020 *J. Mater. Chem. C* **8** 8098
[9] Manchon A, Koo H C, Nitta J, Frolov S M and Duine R A 2015 *Nat. Mater.* **14** 871
[10] Chuang P *et al.* 2015 *Nat. Nanotech.* **10** 35
[11] Katsura H, Nagaosa N and Balatsky A V 2005 *Phys. Rev. Lett.* **95** 057205
[12] Ganichev S D and Golub L E 2014 *Phys. Status Solidi B* **251** 1801
[13] Dresselhaus G 1955 *Phys. Rev.* **100** 580
[14] Shen Y H, Tong W Y, Hu H, Zheng J D and Duan C G 2021 *Chin. Phys. Lett.* **38** 037501
[15] Kuhlen S, Schmalbuch K, Hagedorn M, Schlammes P, Patt M, Lepsa M, Guentherodt G and Beschoten B 2012 *Phys. Rev. Lett.* **109** 146603
[16] Guan Z, Hu H, Shen X, Xiang P, Zhong N, Chu J and Duan C 2020 *Adv. Electron. Mater.* **6** 1900818
[17] Ye Q, Shen Y, Yuan Y, Zhao Y F and Duan C G 2020 *Acta Phys. Sin.* **69** 217710 (in Chinese)
[18] Picozzi S 2014 *Front. Phys.* **2** 00010
[19] Datta S and Das B 1990 *Appl. Phys. Lett.* **56** 665
[20] Di Sante D, Barone P, Bertacco R and Picozzi S 2013 *Adv. Mater.* **25** 509
[21] Liebmann M *et al.* 2016 *Adv. Mater.* **28** 560
[22] Rinaldi C *et al.* 2018 *Nano. Lett.* **18** 2751
[23] da S L G D, Barone P and Picozzi S 2016 *Phys. Rev. B* **93** 245159
[24] Tao L, Paudel T, Kovalev A and Tsymbal E 2017 *Phys. Rev. B* **95** 245141
[25] Arras R, Gosteau J, Zhao H J, Paillard C, Yang Y and Bellaiche L 2019 *Phys. Rev. B* **100** 174415
[26] Wang Y *et al.* 2018 *Mater. Horiz.* **5** 521
[27] Zhou B 2020 *Nanoscale* **12** 5533
[28] Bel'kov V V *et al.* 2008 *Phys. Rev. Lett.* **100** 176806
[29] Karimov O Z, John G H, Harley R T, Lau W H, Flatte M E, Henini M and Airey R 2003 *Phys. Rev. Lett.* **91** 246601
[30] Chen Y, Faelt S, Wegscheider W and Salis G 2014 *Phys. Rev. B* **90** 121304(R)
[31] Tan H X, Li M L, Liu H T, Liu Z R, Li Y C and Duan W H 2019 *Phys. Rev. B* **99** 195434
[32] Ding N, Chen J, Dong S and Stroppa A 2020 *Phys. Rev. B* **102** 165129
[33] Zhang Y, Lin L F, Moreo A, Alvarez G and Dagotto E 2021 *Phys. Rev. B* **103** L121114
[34] Bernevig B A, Orenstein J and Zhang S C 2006 *Phys. Rev. Lett.* **97** 236601
[35] Schliemann J 2017 *Rev. Mod. Phys.* **89** 011001
[36] Altmann P, Walser M, Reichl C, Wegscheider W and Salis G 2014 *Phys. Rev. B* **90** 201306
[37] Kresse G and Furthmuller J 1996 *Phys. Rev. B* **54** 11169
[38] Blöchl P E 1994 *Phys. Rev. B* **50** 17953
[39] Monkhorst H J and Pack J D 1976 *Phys. Rev. B* **13** 5188
[40] King-Smith R D and Vanderbilt D 1993 *Phys. Rev. B* **47** 1651
[41] Resta R 1994 *Rev. Mod. Phys.* **66** 899
[42] Togo A, Oba F and Tanaka I 2008 *Phys. Rev. B* **78** 134106
[43] Krukau A V, Vydrov O A, Izmaylov A F and Scuseria G E 2006 *J. Chem. Phys.* **125** 224106
[44] Jia Y, Zhao M, Gou G, Zeng X C and Li J 2019 *Nanoscale Horiz.* **4** 1113
[45] Shen X W, Tong W Y, Gong S J and Duan C G 2017 *2D Mater.* **5** 011001
[46] Wu M and Zeng X C 2016 *Nano Lett.* **16** 3236
[47] Fei R, Kang W and Yang L 2016 *Phys. Rev. Lett.* **117** 097601
[48] Wang H and Qian X 2017 *2D Mater.* **4** 015042
[49] Ai H, Ma X, Shao X, Li W and Zhao M 2019 *Phys. Rev. Mater.* **3** 054407
[50] Anshory M and Absor M A U 2020 *Physica E* **124** 114372
[51] Kim M, Im J, Freeman A J, Ihm J and Jin H 2014 *Proc. Natl. Acad. Sci. USA* **111** 6900